PCCP

Accepted Manuscript

This is an *Accepted Manuscript*, which has been through the Royal Society of Chemistry peer review process and has been accepted for publication.

Accepted Manuscripts are published online shortly after acceptance, before technical editing, formatting and proof reading. Using this free service, authors can make their results available to the community, in citable form, before we publish the edited article. We will replace this *Accepted Manuscript* with the edited and formatted *Advance Article* as soon as it is available.

You can find more information about *Accepted Manuscripts* in the **Information for Authors**.

Please note that technical editing may introduce minor changes to the text and/or graphics, which may alter content. The journal's standard **Terms & Conditions** and the **Ethical guidelines** still apply. In no event shall the Royal Society of Chemistry be held responsible for any errors or omissions in this *Accepted Manuscript* or any consequences arising from the use of any information it contains.

Constructing atomic layer g-C₃N₄/CdS nanoheterojunction with efficiently enhanced visible light photocatalytic activity

Meiliang Lu, Zengxia Pei, Sunxian Weng, Wenhui Feng, Zhibin Fang, Zuyang Zheng, Mianli Huang and Ping Liu*

Abstract: Ultrathin two dimensional (2D) materials have triggered extensive interest for their exceptional properties and potential application. Herein, the atomic layer graphitic carbon nitride (g-C₃N₄) were obtained by a simple ultrasonic exfoliation approach, and Cadmium sulfide (CdS)
[10] nanoparticles were successfully grown on this ultrathin g-C₃N₄ nanosheet (UCNNS) via a facile solvothermal method. The as-prepared UCNNS/CdS nanocomposites exhibit significantly enhanced photocatalytic activity for methyl orange (MO) degradation under visible light irradiation. The enhancement of the photocatalytic activity should be attribute to the well-matched band structure and imitate contact interfaces between the UCNNS and CdS, which lead to the effective transfer and
[15] separation of photogenerated charge carrier. The mechanism for the composite photodegrade MO was also investigated in this study. This study highlights the potential application of atomic layer g-C₃N₄ based photocatalysts, and we hope our work may provide a new insight for the construction of photocatalysts with efficient visible light activities.

Keywords: two dimensional, atomic layer g-C₃N₄, nanoheterojunction, visible light

[20]

1. Introduction

2D nanosheet materials, which consist of monolayer or a few atomic layers, have aroused broad interest among research areas owing to their unique optical and electronic properties, as well as
[25] their large surface area.[1-5] These merits render 2D nanosheet materials promising potential for catalysis, energy storage, environmental remediation and water splitting applications.[4-8] Among various 2D materials, Graphene, which exhibits superiority in properties such as high carrier mobility, large
[30] specific surface and quantum hall effect, is the most famous and widely investigated one.[2, 3] In particular, the graphene-based photocatalysts generally show remarkably enhanced photocatalytic performance due to the accelerated transfer and promoted separation of photo-generated carriers caused by
[35] graphene.[9-11] However, the pristine graphene by itself is a zero bandgap material and does not have photocatalytic activity, and it just serves as an electron acceptor or transport intermediates in the photocatalytic reaction.[2, 12] In addition, excess graphene will block the incident light and hamper the external quantum
[40] efficiency of the photocatalyst.[13, 14]

Recent years have witnessed the bloom of research into g-C₃N₄. This novel metal-free photocatalyst possesses proper band structure that is suitable for water splitting and photocatalytic degradation of organic pollutants under visible light.[15-19]
[45] Nevertheless, the photocatalytic efficiency of bulk g-C₃N₄ is far from satisfactory for its severe recombination rate of photogenerated charge carriers and relatively small surface area.[20, 21] Noticeably, as a π-conjugated material, g-C₃N₄ has not been much viewed from the perspective of 2D material.[21, 22]
[50] Actually, recent works reported that ultrathin g-C₃N₄ nanosheets obtained from peeling off the bulk counterpart depict fascinating

prospects in improving the transfer and separation of photoexcited charge carriers.[12, 21-24] Compared to the bulk g-C₃N₄, the apparent advantages of ultrathin nanosheets mainly include
[55] three aspects: (1) The specific surface area is bigger than the bulk one, and can provide abundant reactive sites.[21, 22] (2) The ultrathin nanosheets structure can remarkably reduce the distance for the photoexcited carriers to transfer from one place to the interface.[12, 21-23] Therefore, the transportation and separation of
[60] the photogenerated electron-hole pairs is improved. (3) The shift-up conduction and shift-down valence bands of ultrathin nanosheets can strengthen the reduction and oxidation ability of electrons and holes respectively.[23] But before practical applications, the light absorption capacity of g-C₃N₄ still needs
[65] further improvement as this material can only absorb light with wavelength shorter than 460nm, which accounts for a small part of the whole visible light region.[16, 25, 26]

CdS has long been one of the most attractive visible light active semiconductor photocatalysts due to its efficient
[70] absorption of visible light (up to 520 nm or even longer) and suitable bandedge position.[11, 27, 28] In light of this, CdS can act as an excellent photosensitizer in many wide bandgap photocatalysts systems like CdS-TiO₂[29, 30] and CdS-ZnO.[31, 32] Regretfully, there are still two serious barriers that greatly hold back the wide
[75] application of pure CdS. Firstly, the recombination rate of photo-induced electron-hole is undesired high.[11, 17] Worse still, S²⁻ in CdS tend to be oxidized by photoexcited hole upon strong irradiation, which is known as the photocorrosion phenomenon.[27, 33] Hence, numerous works focus on addressing the intrinsic
[80] disadvantages of CdS. Approaches like using sacrificial agent and loading proper co-catalyst have been adopted and were proven to be effective.[11, 33-35] Promisingly, fabricating heterojunctions between two semiconductors is another strategy to tackle with

both these two barriers. By efficaciously transferring the holes from the CdS domain can alleviate the accumulation of holes, thus inhibition of charge carriers' recombination and photocorrosion can be simultaneously achieved.[30, 36] When reviewing the band alignment of CdS and g-C_3N_4, it is fortunate to find that their band edges match quite well to facilitate the separation of e-h pairs. Though some very recent works have demonstrated the validity of the above-mentioned strategy by synthesizing g-C_3N_4/CdS composites via different preparation methods,[17, 33, 37, 38] the unique properties of the atomic layer g-C_3N_4 were unexceptionally not take into account or investigated in-depth in their work. However, the novel characteristics of these ultrathin g-C_3N_4 nanosheets (UCNNS) probably is extremely important for boosting the photocatalytic activity considering the great success in similar graphene coated photocatalysts. Hitherto, there is no report for in situ growth of CdS nanoparticles on UCNNS.

In this study, UCNNS was obtained through a thermal condensation of urea followed by a facile ultrasonic method. CdS nanopaticles were then in situ growing onto the UCNNS to fabricate nano-heterojunctions via a solvothermal method, during which UCNNS provided many binding sites for anchoring CdS nanoparticles. In addition, intimate contacted interfaces between the UCNNS and CdS were also developed. Consequently, the composite exhibits significantly enhanced capability in degradation of MO due to the dramatically promoted charge separation. It was observed that the optimal photocatalytic activity of the composite with 10 wt% UCCNS loading amount is about 6 and 50 times higher than pure CdS and UCNNS for degradation of MO, and the photostability of CdS was also apparently reinforced. Moreover, the active species of the composite for the degradation reaction were investigated systematically. This study highlights the potential application of atomic layer g-C_3N_4 based photocatalysts, and it is hoped that the present work may provide a new insight for construction of stable photocatalysts with efficient visible light activities.

2. Experimental Section

2.1 Materials

All reagents in this work were AR grade and used without further purification. Urea $((NH_2)_2CO)$, cadmium acetate dehydrate $(Cd(CH_3COO)_2 \cdot 2H_2O)$, thioacetamide (TAA), ethyl alcohol and scavengers isopropanol (IPA), ammonium formate (AF), p-benzoquinone (PBQ) were purchased from Sinopharm Chemical Reagent Co. Ltd. (Shanghai, China). Deionized water used in this work was from local sources.

2.2 Synthesis of the Photocatalysts

Metal-free g-C_3N_4 nanosheets was prepared according to a reported method.[20] In detail, 5 g of urea was put into an alumina combustion boat, then was heated to 550℃ with a heating rate of 2 ℃/min and kept at 550℃ for 4 h, followed by cooling to room temperature. The whole process was performed under a helium (He) gas flow (100 mL/min). The product was ground into powder and washed with deionized water. Then as-prepared g-C_3N_4 was collected in the beaker and added in 100ml ethanol. After ultrasonicated for 8 h, the as-prepared g-C_3N_4 was exfoliated into ultrathin g-C_3N_4 nanosheets (UCNNS). When ethanol was evaporated absolutely, and the UCNNS was obtained.

Bulk g-C_3N_4 (BCN) was prepared according to a reported procedure with some modifications.[24] In detail, melamine was heated at 550 ℃ for 4 h under air condition with a ramp rate of 2 ℃/min, and then cooling to room temperature.

UCNNS/CdS composites were synthesized via a one-step procedure. A measured amount of UCNNS were redispersed in a 20 mL ethanol and ultrasonicated again for 1 h. The suspension with 5 mmol $Cd(CH_3COO)_2 \cdot 2H_2O$ was added to a 20-mL ethanol solution，and then was stirred for 5 h to form a homogeneous suspension. After that, a 20-mL ethanol solution with 5 mmol TAA was added to the above mixed suspension and stirred for another 30 min. The obtained suspension was autoclaved in a 100-mL Teflon-lined stainless steel vessel at 180℃ for 12 h. After cooling to room temperature, the as-prepared yellow product was washed by water and ethanol for several times, collected by centrifugation. Finally, the obtained sample was dried in a vacuum oven at 80℃. The UCNNS/CdS composites with weight ratio of UCNNS to CdS were 3, 5, 10, 15 and 20 wt% were marked as 3CN, 5CN, 10CN, 15CN and 20CN, respectively. The 10 wt% BCN/CdS was synthesized by the same procedure without ultrasonicated step, and the obtained product mark as 10BCN.

2.3 Characterization

The crystal structure of as-prepared samples was identified by Bruker D8 ADVANCE X-ray diffractometer (XRD) with a Cu K_α radiation (λ = 0.15418 nm) that operated at 40 kV and 40 mA. The scan rate is 0.05° 2θ s^{-1}. Scanning electron microscope (SEM) images were investigated by a HITACHI SU8000 field-emission scanning electron microscope. The atomic force microscopy (AFM, Nanoscope Multimode IIIa microscope, Veeco Instrument) was used to observe the thickness of the 2D g-C_3N_4 nanosheets. Transmission electron microscopy (TEM, TecnaiG2 F20 S-TWIN, FEI company) with a field emission gun that operated at 200 kV was used to investigate the morphologies of samples. The infrared spectroscopy (IR) analyses were performed on a Nicolet Nexus 670 FT-IR spectrometer. X-ray photoelectron spectroscopy (XPS) analysis was done on an ESCALAB 250 photoelectron spectroscopy (Thermo Fisher Scientific) with a Al K_α X-ray beam (1486.6 eV). Total organic carbon (TOC) measurements of the degradation solution after 16 min of irradiation were operated on a TOC analyzer (TOC-VCPH, Shimadzu). Varian Cary-500 spectrophotometer with $BaSO_4$ as a reference was employed to get the Diffuse reflection spectra (DRS) of the samples. The photoluminescence (PL) spectra were carried out on a Varian Cary-Eclipse 500 with an excitation wavelength at 325 nm. The nitrogen adsorption and desorption isotherms were done on a Micrometrics ASAP 2020 analyzer. The degassing process was hold at 180℃ for 5 h. The electrochemical analysis were conducted on a ZENNIUM electrochemical workstation (Zahner, Germany) with a conventional three-electrode system. The reference and counter electrodes were Ag/AgCl electrode and Pt plate electrode, respectively, and 0.2 M Na_2SO_4 (pH=6.8) aqueous solution was served as electrolyte. The 5mg as-prepared sample was dispersed in 0.5 mL N,N-dimethyl formamide (DMF) solution by

sonication, and then slurry was evenly spread onto FTO glass substrates to served as a working electrode. A 300 W xenon lamp was used to provide visible light source which equipped with a UV cut off filter (λ≥420nm). For electrochemical impedance
5 spectra (ESI) measurement, the amplitude of the sinusoidal wave was 10 mV, and the frequency ranges from 4 MHz to 0.01 Hz.

2.4 Photocatalytic activity test

The photocatalytic activity of as-prepared samples was evaluated by photodegradation of MO with a concentration of 5 mg/L under
10 visible light. The PLS-SXE 300 lamp (Beijing Perfect light Co., Ltd.), which with a UV cut-off filter (λ≥420nm) was served as light source. 30 mg of the photocatalysts was added into a quartz vial with a 80-mL MO solution (5 mg/L). Before the irradiation, the suspension was stirred for 30 min in the dark to established an
15 adsorption/desorption equilibrium. During the irradiation period, 3 ml of the solution was quickly extracted at a definite time interval. After that, the solution was centrifuged at 12000 rpm to remove the catalysts completely and analyzed on a UV-vis spectrometer (Cary-50, Varian Co.).
20 The recycling photocatalytic activity test was performed as follows. After 1st run reaction, the catalyst washed clean, and collected for next run reaction. In similar, the 3rd cycle and 4th run were carried out. The controlled activity experiments were performed similar to the above photocatalytic activity experiment
25 with different radical scavengers added into the reaction system.

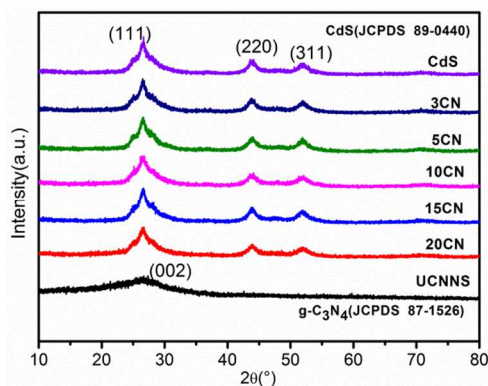### 3. Results and discussion

Figure 1. XRD patterns of pure CdS, pure UCNNS, and UCNNS/CdS composites

30 Fig.1 shows the XRD patterns of pure CdS, pure UCNNS and their composites with different content of UCNNS. For pure g-C_3N_4, the distinct diffraction peak at 27.4°, corresponding to the (002) peak in JPCDS 87-1526, represents the interlayer stacking of the conjugated aromatic groups. The weak peak, corresponding
35 to the (100) plane at about 13°, is attributed to the in-plane structural of tri-s-triazine units. [20, 22, 39] (see in Fig. S1). Compared with the BCN, both of the (002) peak and (100) peak of UCNNS display a markedly reduced intensity and broadened width. It indicates that the interlayer structure of UCNNS was destroyed.
40 This is in agreement with the g-C_3N_4 nanosheets which reported in the literature.[20, 22, 39-41] In addition, the layer number of g-C_3N_4 nanosheet can be evaluated from the (002) diffraction by Scherrer formula.[42, 43] According to the Scherrer formula, the average

thickness of UCNNS is estimated to be 1.0 nm. Therefore, the
45 layer number of UCNNS is about 2-3 layer,[24, 44] and this can be further confirmed by TEM and AFM, which will be discussed later. The XRD pattern of pure CdS possesses the three discernible diffraction peaks at 26.6°, 43.9° and 52.0°, which attributed to the (111), (220) and (311) peaks of face-centered
50 cubic structure of CdS (JCPDS 89-0440). The XRD patterns of UCNNS/CdS composites show no difference with pure CdS due to the low X-ray diffraction intensity of g-C_3N_4 nanosheets and overlapped characteristic peaks with CdS. Nevertheless, the presence of g-C_3N_4 nanosheets in composites can be confirmed
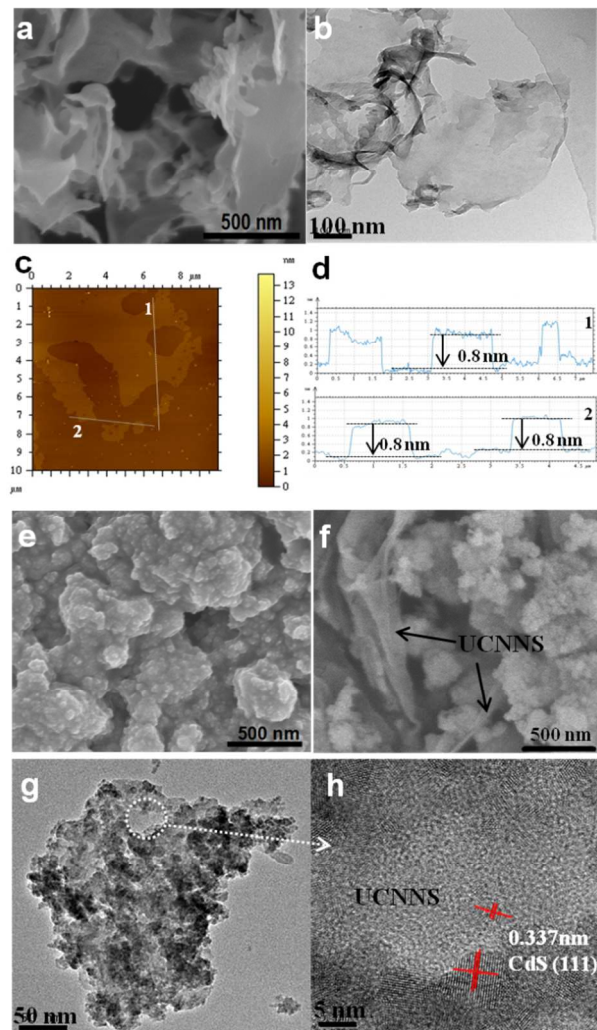55 by SEM, TEM, FTIR and XPS analyses.

Figure 2. (a) SEM image and (b) TEM image of pure UCNNS. (c) AFM image and (d) corresponding thickness analysis of pure UCNNS. (e) SEM image of pure CdS, (f) SEM image of 10CN sample. (g)TEM image and
60 (h) HRTEM image of circle part in (g) for10CN sample.

The detailed morphologies and crystal structures of the UCNNS, CdS and as-prepared composites were directly analyzed by SEM and TEM/HRTEM. As shown in Fig. 2a, the pure g-C_3N_4 displays nanosheets with a laminar structure. In the TEM
65 image (Fig. 2b and Fig. S2), the UCNNS looks like silk veil, which is similar to graphene or graphene oxide that reported,[3, 45] they look transparent due to their thin nature. And the thickness

of g-C_3N_4 nanosheet can be further determined by atomic force microscope (AFM) analyses. Fig. 2c-d reveal that average thickness of the obtained g-C_3N_4 nanosheets is approximately 0.8 nm, which indicates that the g-C_3N_4 nanosheets are composed of only about two C−N layers.[24, 44] Compared with the as-prepared bulk g-C_3N_4 which consist of irregular thick block material (Fig. S3), it is apparently that as-prepared UCNNS possess the larger specific surface area (see Table S1). The morphological feature of bare CdS nanoparticles was investigated by SEM, as shown in Fig. 2e, CdS nanoparticles are significantly aggregated together to be clusters. As shown in the Fig. 2f, after introducing CdS through the solvothermal approach, the CdS nanoparticles dispersed on the UCNNS. The TEM and HRTEM images (Fig.2g-h) intuitively present that the UCNNS were decorated with CdS nanoparticles, and lattice spacing of 0.337 nm can be assigned to the (111) crystal face of CdS (JCPDS 89-0440). These results indicate that CdS nanoparticles are spreading on UCNNS to form nanoheterojunctions. The 2D g-C_3N_4 nanosheets can provide the anchor sites to immobilized the CdS, which can partially prevent the aggregation of CdS nanoparticles.[11] After formation of the nano-heterojunction, the specific surface area of the composites increase in some extent compared with the CdS (see Fig. S7 and Table S1). Based on the above results, the mechanism for the fabrication of UCNNS/CdS composites can be proposed as illustrated in Scheme 1.
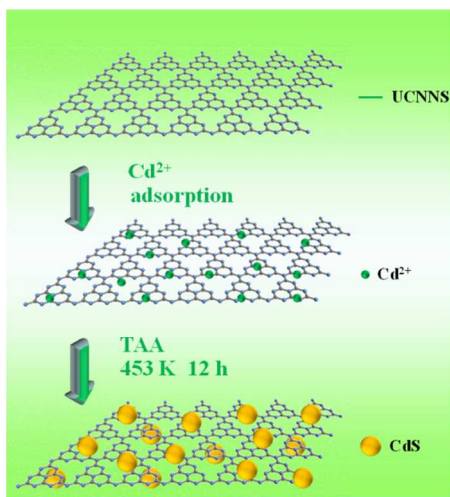
Scheme 1. Mechanism for the formation of UCNNS/CdS nanocomposites

For investigating the interaction between CdS and UCNNS, FTIR instrument was carried out. The FTIR spectroscopy of pure CdS, pure UCNNS, and UCNNS/CdS composite were compared in Fig. 3. For CdS, the peaks between 1100 and 1650 cm^{-1} are ascribed to the Cd-S bond. And the band at 1618 cm^{-1} is attributed to the O-H bending vibration of surface-absorbed water molecule. For pure UCNNS, the characteristic peaks that appearing around 1246, 1316, 1422, 1569, 1641 cm^{-1}, can be assigned to the typical stretching modes of CN heterocycles in g-C_3N_4.[12, 41] The representative breathing mode of triazine units in pure g-C_3N_4 nanosheets can be observed at 813 cm^{-1}.[12, 17, 41] After constructing the nanojunctions between CdS and UCNNS, all the characteristic bands of CdS present in composites because of its high percentage. Additionally, the characteristic peaks for g-C_3N_4

nanosheets also can be observed in composites. The characteristic bands of g-C_3N_4 are gradually heightened with the increase of g-C_3N_4 nanosheets ratio in the composites. As shown in Fig. S8, the corresponding peaks for C-N stretching vibration mode and triazine units for mixed-10CN sample show no discrepance with the pure UCNNS. The mixed-10CN sample, which represents that UCNNS simply mechanical mixing with CdS. For 10CN, a 10 cm^{-1} of red shift occurred at 813 cm^{-1}, and relevant FTIR band for C-N stretching vibration is also weaker than mixed-10CN. It indicates that the interaction may developed between UCNNS and CdS, which weaken the force between C and N atoms. The FTIR results of as-prepared samples are well in accordance with the SEM and TEM/HRTEM, all these indicate that the UCNNS/CdS composites are successfully obtained.
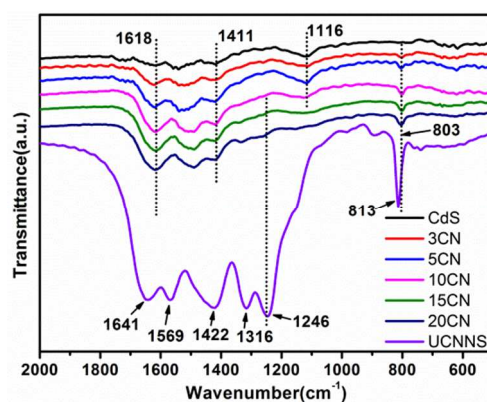

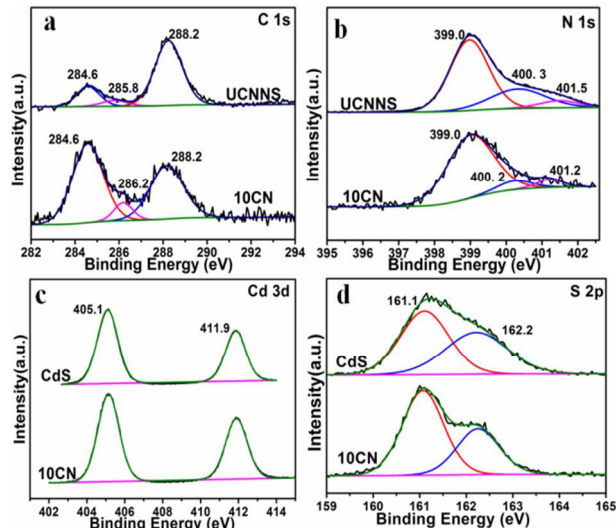**Figure 3.** FTIR spectra of CdS, UCNNS, and UCNNS/ CdS nanocomposites

Figure 4. XPS spectra of (a) C 1s, (b) N 1s. (c) Cd 3d, (d) S 2p for samples.

To further confirm the existence of g-C_3N_4 in composites and study their surface chemical state, XPS measurements were done. Fig. 4a-d indicate that 10CN sample contains C, N, Cd and S element. For UCNNS sample, the C 1s peak can be fitted with three peaks at 284.6 eV, 285.8 eV and 288.2 eV (Fig. 4a top). The peak at 284.6 eV is related to surface adventitious carbon.[39] The peak centered at 288.2 eV can be attributed to the sp^2 bonded to the N-containing aromatic rings (N−C=N), which manifests the

carbon species in the g-C$_3$N$_4$.[33, 38] The small peak (285.8 eV) is ascribed to the sp^3-bonded carbon species from the defects on the g-C$_3$N$_4$ surface. [33, 38] Three peaks at 399.0 eV, 400.3 eV and 401.5eV, can be identified for N 1s spectrum for UCNNS (Fig. 4b top). The binding energy of 399.0 eV is derived from the sp^2-bonded N in the triazine units (C−N=C) in g-C$_3$N$_4$. The weak peaks at 400.3 and 401.5eV originate from the tertiary nitrogen N−(C)$_3$ units and the amino groups (C−N−H), respectively.[33, 37, 38, 46] From Fig. 4a and 4b, we can see that peak (285.8 eV) for C 1s shift to high binding energy when combine UCNNS with CdS, and the two peaks at 400.3 and 401.5eV for N 1s shift to lower binding energy. The shift of binding energy suggests an electronic interaction between UCNNS and CdS,[47] which is consistent with the IR result. In Fig. 4c-d, the XPS peaks at 405.1 and 411.9 eV, and peaks at 161.1 and 162.2 eV, are ascribed to Cd 3d and S 2p in 10CN and bare CdS samples.[33, 37, 38]

The optical performances of as-prepared samples were investigated by UV-vis diffuse reflectance spectroscope (DRS). As shown in Fig. 5, the absorption edge for pure UCNNS is about 420 nm, which is shorter than that 450 nm of as-prepared BCN. This blue-shift is caused by the quantum size confinement effect when reducing the dimensionality of material.[25] The absorption band edge of pure CdS is 520 nm, which enable to sensitize UCNNS to strengthen the optical response.[17] All the as-prepared nanocomposites show broader absorption in the visible region compare to UCNNS, and slight narrower absorption than CdS. These observations for composites are attributed to the interaction between CdS and UCNNS.[37] And the interaction probably play a significant role for improving the separation of the photogenerated electron-hole pairs to enhance the photocatalytic activities. As a result, the composites may lead to a higher photocatalytic activity than pure UCNNS and CdS .
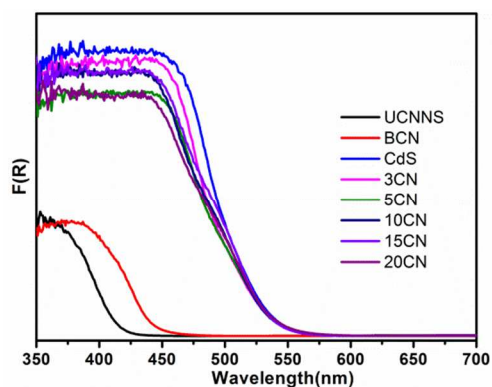

Figure 5. UV-vis spectra of as-prepared samples

The photocatalytic performance of CdS/UCNNS composites were evaluated via MO photodegradation tests under visible light (λ≥420 nm) illumination. Each of the photodegradation reactions was carried out after 30 min adsorption equilibrium in the absence of light condition. Photocatalytic activities for each photocatalyst are demonstrated in Fig. 6a. As we can see in the figure, the activity for BCN is the weakest, almost no MO is decomposed after 16 min visible light irradiation. And photoactivity for UCNNS is a little better than BCN due to the larger specific surface area, but the photocatalytic ability on organic pollution is still weak for its limited light absorption

capacity. The composite photocatalysts reveal the notably enhanced photoactivity for MO degradation compared to the bare UCNNS and CdS. In our research system, the optimal activity was achieved at 10CN sample, which almost eliminate MO completely after 16-min irradiation (see Fig. S3 and S6). As depicted in Fig. 6b, the photoactivity of 10CN sample is about 6 and 50 times higher compared to CdS and UCNNS respectively. Specific surface area is always a crucial factor in photocatalysis. To describe the photocatalytic performance more exactly, the reaction rate for photocatalytic degradation before and after normalization with surface area is compared (see Fig. S12). After normalization with surface area, 10CN still exhibits the remarkable higher photocatalytic activity compared to 10BCN, which convincingly demonstrates the advantage of 2D g-C$_3$N$_4$ nanosheets hybrid photocatalyst than the bulk one. These results suggest that the synergic effect between the CdS and UCNNS probably play a pivotal role for accelerating the transfer and separation of the charge carriers to improve the photocatalytic activity. And this can be certified through further research.
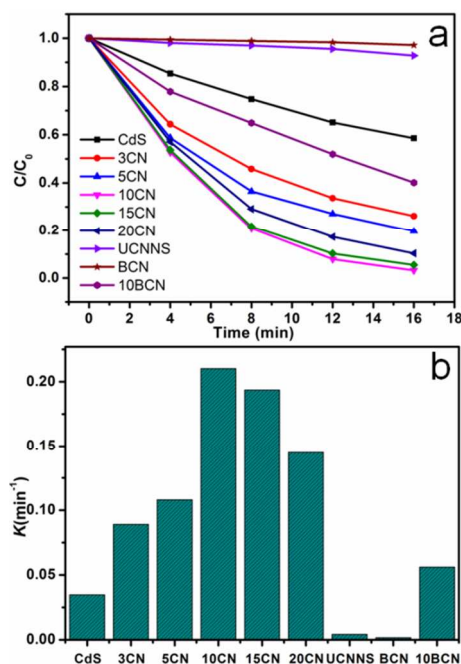

Figure 6. (a) Photocatalytic degradation of MO over the as-prepared samples under visible light illumination (λ≥420 nm). (b) The corresponding rate constant *k* of different as-prepared samples.

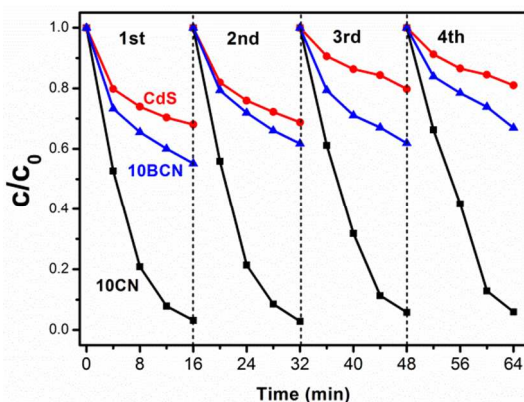**Figure 7.** Cycling photocatalytic degradation of MO over UCNNS/CdS composites under visible light irradiation (λ≥420 nm).

The stability of as-prepared samples were evaluated via a recycling test under the visible light illumination. From Fig. 7, the photocatalytic activity of CdS decreases gradually during the cycling test due to its photocorrosion under irradiation. Meanwhile, 10BCN also exhibits a slower decrease of photocatalytic performance. No noticeable decrease of photocatalytic activity for 10CN after four successive cycles of reaction. In addition, as shown in Fig. S9-10, neither the structure or the morphology of 10CN sample changed after recycling test, which indicates that the 10CN sample is stable during the photocatalytic reaction. These result indicates that UCNNS/CdS composite not only significantly enhance the photocatalytic activity, but also can effectively restrain the photocorrosion of the CdS. The 10CN reveals more stable than 10BCN, which also suggest that the 2D g-C$_3$N$_4$ nanosheets is superior to the bulk one to stabilize the CdS.
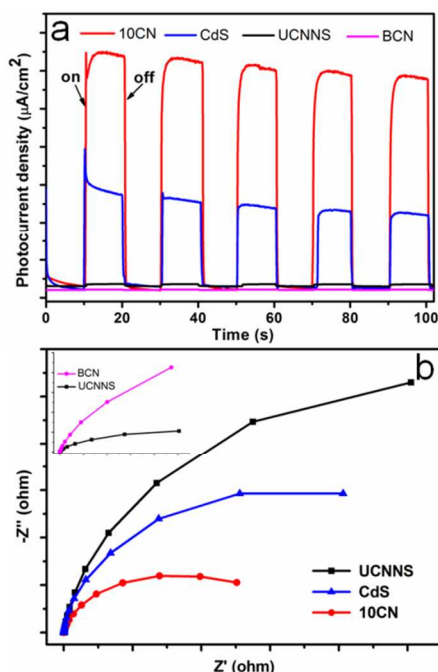

Figure 8. Photoelectrochemical properties of the as-prepared CdS, UCNNS, BCN and 10CN samples. (a) Transient photocurrent response under visible light irradiation (λ≥420 nm) and (b) ESI Nyquist plots of samples, inset image is comparison for BCN and UCNNS.

Based on the aforementioned experiment results, we believe that the enhancement of photocatalytic activity for UCNNS/CdS composite is credited to the efficiently interfacial transfer and separation of photogenerated carriers between g-C$_3$N$_4$ nanosheets and CdS particles. This assumption can be verified by photoelectrochemical measurements. Fig. 8a shows the transient photocurrent response of 10CN, CdS, UCNNS, and BCN under visible light irradiation for several on-off cycles. From Fig. 8a, we can clearly see that photocurrent response of BCN is lower than the UCNNS, 10CN is significantly higher than that of the UCNNS and CdS under the same visible light illumination. The generation of photocurrent is mainly result in the photoinduced electrons diffuse to the ITO.[48] Therefore, the enhanced

photocurrent implies that more effective charge transfer and separation is achieved after constructing the heterojunctions. The strength of the photocurrent is in line with the order of photocatalytic activities. For further identify the above results, electrochemical impedance spectra (EIS), a useful measurement to characterize the charge carriers transportation, was also performed. Fig. 8b displays that the impedance arc radius of UCNNS is smaller than BCN, which indicated a smaller charge transfer resistance for the ultrathin g-C$_3$N$_4$. 10CN is much smaller than bare CdS and g-C$_3$N$_4$ nanosheets, which reflects a decreased charge transfer resistance across the interface[49, 50] between CdS and UCNNS. Therefore, the remarkably improved life-time and more efficient separation of photoexcited carriers induce a notable enhancement of the photocatalytic activity in MO degradation.

Both the images of the composites and above results suggest that the enhanced photocatalytic activity is attributed to the interfacial transfer of the photogenerated charges between the UCNNS and CdS. This transfer is also investigated by photoluminescence (PL) measurements. Fig. 9 presents the PL spectra for the BCN, UCNNS, and the 10CN samples. The BCN sample shows a strong emission peak that centered at about 465 nm, which can be assigned to the recombination of electron and holes in g-C$_3$N$_4$. In comparison, the emission intensity of the UCNNS decrease clearly, which reveals that ultrathin g-C$_3$N$_4$ own a rapid charge transfer than the bulk one. When the CdS nanoparticles are added, the PL drops remarkably. The reduction of the PL can be interpreted as the efficient transfer of the photoinduced electrons and holes between the UCNNS and CdS.
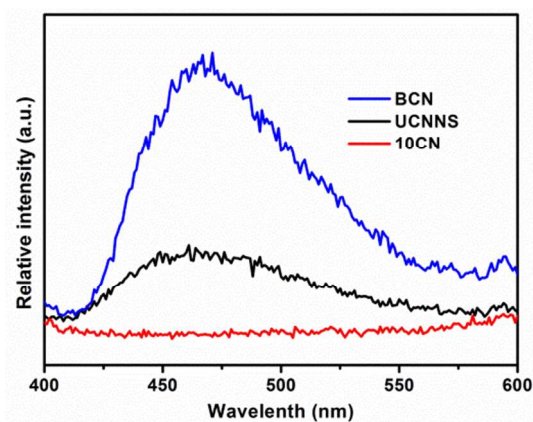

Figure 9. Comparison of PL spectra for BCN,UCNNS, and 10CN samples excitated at 325 nm.

In order to understand the role of photoexcited active species in degradation of dye MO, a succession of control experiments were performed. The different scavengers aiming at hydroxyl radicals (·OH), holes (h$^+$), superoxide radicals (·O$_2^-$) were added in degradation process. Herein, isopropanol (IPA)[51, 52] is used to scavenge ·OH, ammonium formate (AF) is for h$^+$,[35] and p-benzoquinone (PBQ) is for ·O$_2^-$.[53, 54] Fig. 10 presents the photocatalytic activities of 10CN sample with adding the different scavengers. It is clearly that when PBQ was added into the reaction system, the degradation of MO is almost terminated. And when AF is added, the degradation is apparently inhibited. Thus, it can be concluded that the superoxide radicals play the

most pivotal role in degradation of dye MO, the $\cdot O_2^-$ and h^+ are the main active species that affecting the degradation rate.
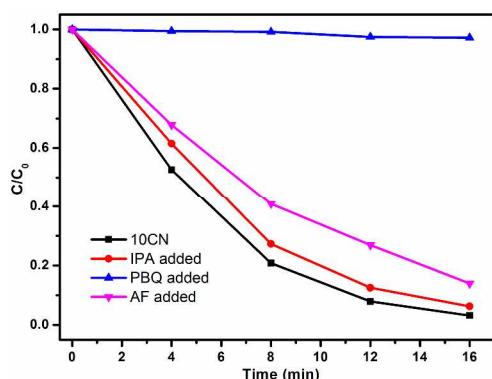

Figure 10. Effects of different scavenger addition on the photocatalyzed degradation of MO for 10CN sample.

On the basis of the above experiments and results, a tentative mechanism for the degradation of MO onto the UCNNS/CdS nanocomposite is illustrated in Fig. 11. Both UCNNS and CdS can generate the photoexcited holes and electrons under visible light irradiation. It is reported that the conduction band (CB) and valance band (VB) of CdS are lower than that of g-C$_3$N$_4$. After constructing the nanoheterostructure, the photoinduced electrons on CB of UCNNS can directly migrate to CdS, while the holes on VB of CdS can transfer to VB to UCNNS. Thus, the separation efficiency of electron-hole pairs is improved in a large extent, and the photocorrosion of CdS by holes is greatly alleviated, leading to a remarkable enhancement of photocatalytic activity.
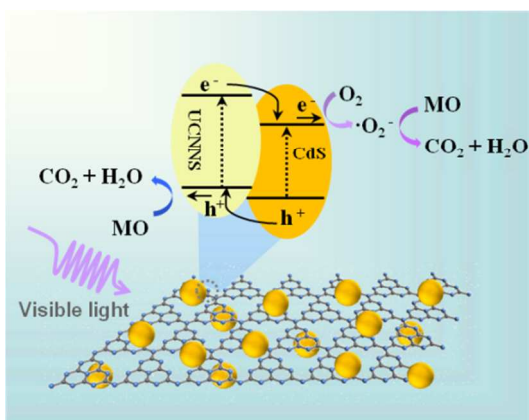

Figure 11. Schematic diagram of photogenerated electrons and holes transfer in UCNNS/CdS composites and photocatalytic degradation of MO under visible light irradiation (($\lambda \geq 420$ nm)

Conclusions

In summary, the atomic layer g-C$_3$N$_4$ can be obtained through a thermal condensation of urea and a simple ultrasonic method. The UCNNS/CdS nanocomposites were successfully synthesized by a simple solvothermal method. The photoactivity of MO degradation under visible light irradiation is significantly enhanced after constructing the heterostructure between UCNNS and CdS. The result also indicates that such a 2D UCNNS can provide more binding site than the bulk one to anchored CdS nanoparticle which own a better photoactvity. In addition, the as-

prepared composites is stable during the photocatalytic reaction. Both the photostability and enhanced photocatalytic activity of the composite can be explained by the effective transfer and separation of photogenerated charge carriers between the CdS and UCNNS. Furthermore, superoxide radicals play the most pivotal role in degradation of dye MO. This study highlights the potential application of ultrathin g-C$_3$N$_4$ nanosheets hybrid photocatalysts, and we hope that it may provide a new insight for the construction of stable photocatalysts that with efficient visible light activities.

Notes and references

State Key Laboratory Breeding Base of Photocatalysis, Research Institute of Photocatalysis, Fuzhou University, Fuzhou 350002, P. R. China. Fax: +86-591-8377-9239; Tel:+86-591-8377-9239; Email: liuping@fzu.edu.cn

† Supporting Information available: [TEM; SEM; UV-visible absorption spectra; BET and so on].

1. K. S. Novoselov, D. Jiang, F. Schedin, T. J. Booth, V. V. Khotkevich, S. V. Morozov and A. K. Geim, *Proc. Natl. Acad. Sci. U. S. A*, 2005, **102**, 10451-10453.
2. X. Huang, X. Qi, F. Boey and H. Zhang, *Chem. Soc. Rev.*, 2012, **41**, 666-686.
3. Q. Xiang, J. Yu and M. Jaroniec, *Chem. Soc. Rev.*, 2012, **41**, 782-796.
4. A. Anto Jeffery, C. Nethravathi and M. Rajamathi, *J. Phys. Chem. C*, 2014, **118**, 1386-1396.
5. H. C. Yongfu Sun, Shan Gao, Zhihu Sun, Qinghua Liu, Qin Liu, Fengcai Lei, Tao Yao, and S. W. Jingfu He, and Yi Xie, *Angew. Chem. Int. Ed.* , 2012, **51**, 8727 –8731.
6. L. Peng, X. Peng, B. Liu, C. Wu, Y. Xie and G. Yu, *Nano Lett.*, 2013, **13**, 2151-2157.
7. Y. Yao, Z. Lin, Z. Li, X. Song, K.-S. Moon and C.-p. Wong, *J. Mater. Chem.*, 2012, **22**, 13494.
8. J. N. Coleman, M. Lotya, A. O'Neill, S. D. Bergin, P. J. King, U. Khan, K. Young, A. Gaucher, S. De, R. J. Smith, I. V. Shvets, S. K. Arora, G. Stanton, H. Y. Kim, K. Lee, G. T. Kim, G. S. Duesberg, T. Hallam, J. J. Boland, J. J. Wang, J. F. Donegan, J. C. Grunlan, G. Moriarty, A. Shmeliov, R. J. Nicholls, J. M. Perkins, E. M. Grieveson, K. Theuwissen, D. W. McComb, P. D. Nellist and V. Nicolosi, *Science*, 2011, **331**, 568-571.
9. W. H. Feng, Z. X. Pei, Z. B. Fang, M. L. Huang, M. L. Lu, S. X. Weng, Z. Y. Zheng, J. Hu and P. Liu, *J. Mater. Chem. A*, 2014, **2**, 7802-7811.
10. B. Weng, S. Liu, N. Zhang, Z.-R. Tang and Y.-J. Xu, *J. Catal.* , 2014, **309**, 146-155.
11. Q. Li, B. Guo, J. Yu, J. Ran, B. Zhang, H. Yan and J. R. Gong, *J. Am. Chem. Soc.* , 2011, **133**, 10878-10884.
12. H. Xu, J. Yan, X. She, L. Xu, J. Xia, Y. Xu, Y. Song, L. Huang and H. Li, *Nanoscale*, 2014, **6**, 1406.
13. N. Zhang, M. Q. Yang, Z. R. Tang and Y. J. Xu, *ACS nano*, 2014, **8**, 623-633.
14. Y. Zhang, Z. R. Tang, X. Fu and Y. J. Xu, *ACS nano*, 2010, **4**, 7303-7314.
15. X. Wang, K. Maeda, A. Thomas, K. Takanabe, G. Xin, J. M. Carlsson, K. Domen and M. Antonietti, *Nat. Mater.*, 2009, **8**, 76-80.
16. G. Zhang, M. Zhang, X. Ye, X. Qiu, S. Lin and X. Wang, *Adv. Mater.*, 2014, **26**, 805-809.

17. J. Fu, B. Chang, Y. Tian, F. Xi and X. Dong, *J. Mater. Chem. A*, 2013, **1**, 3083.

18. G. Liao, S. Chen, X. Quan, H. Yu and H. Zhao, *J J. Mater. Chem.*, 2012, **22**, 2721.

19. Y. Hou, A. B. Laursen, J. Zhang, G. Zhang, Y. Zhu, X. Wang, S. Dahl and I. Chorkendorff, *Angew. Chem. Int. Ed. Engl.*, 2013, **52**, 3621-3625.

20. Y. Hou, Z. Wen, S. Cui, X. Guo and J. Chen, *Adv. Mater.*, 2013, **25**, 6291-6297.

21. P. Niu, L. Zhang, G. Liu and H.-M. Cheng, *Adv. Funct. Mater.*, 2012, **22**, 4763-4770.

22. S. Yang, Y. Gong, J. Zhang, L. Zhan, L. Ma, Z. Fang, R. Vajtai, X. Wang and P. M. Ajayan, *Adv. Mater.*, 2013, **25**, 2452-2456.

23. J. Xu, L. Zhang, R. Shi and Y. Zhu, *J. Mater. Chem. A*, 2013, **1**, 14766.

24. X. Zhang, X. Xie, H. Wang, J. Zhang, B. Pan and Y. Xie, *J. Am. Chem. Soc.*, 2013, **135**, 18-21.

25. M. Zhang and X. Wang, *Energy Environ. Sci.*, 2014, **7,** 1902-1906.

26. Y. Chen, J. Zhang, M. Zhang and X. Wang, *Chem. Sci.*, 2013, **4**, 3244.

27. Y. Hu, X. Gao, L. Yu, Y. Wang, J. Ning, S. Xu and X. W. Lou, *Angew. Chem. Int. Ed. Engl.*, 2013, **52**, 5636-5639.

28. Y. Zhang, Y. Tang, X. Liu, Z. Dong, H. H. Hng, Z. Chen, T. C. Sum and X. Chen, *Small*, 2013, **9**, 996-1002.

29. S. Qian, C. Wang, W. Liu, Y. Zhu, W. Yao and X. Lu, *J. Mater. Chem.*, 2011, **21**, 4945.

30. Z. Chen and Y.-J. Xu, *ACS Appl. Mater. Interfaces*, 2013, **5**, 13353-13363.

31. X. Wang, L. Yin, G. Liu, L. Wang, R. Saito, G. Q. Lu and H.-M. Cheng, *Energy Environ. Sci.*, 2011, **4**, 3976.

32. Y. Tak, H. Kim, D. Lee and K. Yong, *Chem. Commun.*, 2008, 4585-4587.

33. J. Zhang, Y. Wang, J. Jin, J. Zhang, Z. Lin, F. Huang and J. Yu, *ACS Appl. Mater. Interfaces*, 2013, **5**, 10317-10324.

34. H. Y. Xu Zong, Guopeng Wu, Guijun Ma, Fuyu Wen, Lu Wang, and Can Li, *J. Am. Chem. Soc.*, 2008, **130**, 7176-7177.

35. Z. Chen, S. Liu, M. Q. Yang and Y. J. Xu, *ACS Appl. Mater. Interfaces*, 2013, **5**, 4309-4319.

36. Z. Liu, B. Wu, Y. Zhu, F. Wang and L. Wang, *J. Colloid Interf. Sci.*, 2013, **392**, 337-342.

37. L. Ge, F. Zuo, J. Liu, Q. Ma, C. Wang, D. Sun, L. Bartels and P. Feng, *J. Phys. Chem. C*, 2012, **116**, 13708-13714.

38. S.-W. Cao, Y.-P. Yuan, J. Fang, M. M. Shahjamali, F. Y. C. Boey, J. Barber, S. C. Joachim Loo and C. Xue, *Int. J. Hydrogen Energ.*, 2013, **38**, 1258-1266.

39. D. Gao, Q. Xu, J. Zhang, Z. Yang, M. Si, Z. Yan and D. Xue, *Nanoscale*, 2014, **6**, 2577.

40. F. Dong, L. Wu, Y. Sun, M. Fu, Z. Wu and S. C. Lee, *J. Mater. Chem.*, 2011, **21**, 15171.

41. H. Zhao, H. Yu, X. Quan, S. Chen, Y. Zhang, H. Zhao and H. Wang, *Appl. Catal. B: Environ.*, 2014, **152-153**, 46-50.

42. C. N. R. Rao, K. Biswas, K. S. Subrahmanyam and A. Govindaraj, *J. Mater. Chem.*, 2009, **19**, 2457.

43. B. Saner, F. Okyay and Y. Yürüm, *Fuel*, 2010, **89**, 1903-1910.

44. H. Zhao, H. Yu, X. Quan, S. Chen, H. Zhao and H. Wang, *RSC Adv.*, 2014, **4**, 624.

45. T.-F. Yeh, J.-M. Syu, C. Cheng, T.-H. Chang and H. Teng, *Adv. Funct. Mater.*, 2010, **20**, 2255-2262.

46. L. Ge, C. Han and J. Liu, *J. Mater. Chem.*, 2012, **22**, 11843.

47. J. X. Sun, Y. P. Yuan, L. G. Qiu, X. Jiang, A. J. Xie, Y. H. Shen and J. F. Zhu, *Dalton Trans.*, 2012, **41**, 6756-6763.

48. S. Weng, B. Chen, L. Xie, Z. Zheng and P. Liu, *J. Mater. Chem. A*, 2013, **1**, 3068.

49. H. Zhang, R. Zong and Y. Zhu, *J. Phys. Chem. C*, 2009, **113**, 4605-4611.

50. Z. Pei, L. Ding, J. Hu, S. Weng, Z. Zheng, M. Huang and P. Liu, *Appl. Catal. B: Environ.*, 2013, **142-143**, 736-743.

51. Y. Park, Y. Na, D. Pradhan, B.-K. Min and Y. Sohn, *CrystEngComm*, 2014, **16**, 3155.

52. W. J. Kim, D. Pradhan, B.-K. Min and Y. Sohn, *Appl. Catal. B: Environ.*, 2014, **147**, 711-725.

53. L. Shi, L. Liang, J. Ma, F. Wang and J. Sun, *Dalton Trans.*, 2014, **43**, 7236-7244.

54. M. Q. Yang, Y. Zhang, N. Zhang, Z. R. Tang and Y. J. Xu, *Sci. Rep.*, 2013, **3**, 3314.